Geophysical Research Letters

RESEARCH LETTER
10.1029/2020GL087348

Weakening of the Extratropical Storm Tracks in Solar Geoengineering Scenarios

Charles G. Gertler[1], Paul A. O'Gorman[1], Ben Kravitz[2,3], John C. Moore[4,5], Steven J. Phipps[6], and Shingo Watanabe[7]

[1]Department of Earth, Atmospheric and Planetary Sciences, Massachusetts Institute of Technology, Cambridge, MA, USA, [2]Department of Earth and Atmospheric Sciences, Indiana University, Bloomington, IN, USA, [3]Atmospheric Sciences and Global Change Division, Pacific Northwest National Laboratory, Richland, WA, USA, [4]College of Global Change and Earth System Science, Beijing Normal University, Beijing, China, [5]Arctic Centre, University of Lapland, Rovaniemi, Finland, [6]Institute for Marine and Antarctic Studies, University of Tasmania, Hobart, Australia, [7]Japan Agency for Marine-Earth Science and Technology (JAMSTEC), Yokohama, Japan

Key Points:
- Northern Hemisphere extratropical storm track weakens in response to increased CO_2 even with the use of solar geoengineering
- Southern Hemisphere extratropical storm track also weakens in a solar geoengineering scenario but strengthens under global warming
- Storm-track intensity changes in all cases are related to changes in mean temperature structure and moisture

Supporting Information:
- Supporting Information S1

Correspondence to:
C. G. Gertler,
cgertler@mit.edu

Citation:
Gertler, C. G., O'Gorman, P. A., Kravitz, B., Moore, J. C., Phipps, S. J., & Watanabe, S. (2020). Weakening of the extratropical storm tracks in solar geoengineering scenarios. *Geophysical Research Letters*, *47*, e2020GL087348. https://doi.org/10.1029/2020GL087348

Received 31 JAN 2020
Accepted 14 APR 2020
Accepted article online 23 APR 2020

Abstract Solar geoengineering that aims to offset global warming could nonetheless alter atmospheric temperature gradients and humidity and thus affect the extratropical storm tracks. Here, we first analyze climate model simulations from experiment G1 of the Geoengineering Model Intercomparison Project, in which a reduction in incoming solar radiation balances a quadrupling of CO_2. The Northern Hemisphere extratropical storm track weakens by a comparable amount in G1 as it does for increased CO_2 only. The Southern Hemisphere storm track also weakens in G1, in contrast to a strengthening and poleward shift for increased CO_2. Using mean available potential energy, we show that the changes in zonal-mean temperature and humidity are sufficient to explain the different responses of storm-track intensity. We also demonstrate similar weakening in a more complex geoengineering scenario. Our results offer insight into how geoengineering affects storm tracks, highlighting the potential for geoengineering to induce novel climate changes.

Plain Language Summary Solar geoengineering refers to reflecting incoming sunlight to counteract the greenhouse effect of increased carbon dioxide concentrations and is one proposed intervention to avoid the most dramatic risks of global warming. Climate under solar geoengineering would nonetheless be meaningfully different from a baseline climate without increased carbon dioxide. The extratropical storm tracks, regions with heightened incidence of extratropical cyclones, are important components of weather and climate outside of the tropics. In simulations with global climate models, we find that the storm track in the Northern Hemisphere is similarly weakened in a solar geoengineering scenario with little change in global mean temperature as in a global warming scenario. The storm track in the Southern Hemisphere also weakens in the geoengineering scenario in contrast to a strengthening with global warming. The weakening of the storm tracks in the geoengineering scenario is partly related to a weakening of the pole-to-equator temperature gradient in both hemispheres. This means that reflecting incoming sunlight may not prevent changes in the strength of extratropical cyclones in the Northern Hemisphere and may overcorrect in the Southern Hemisphere.

1. Introduction

Active management of the Earth's climate through solar geoengineering, in which incoming shortwave radiation is reflected to counteract the longwave radiative forcing from greenhouse gasses, is one proposed mechanism to avert dangerous global warming due to anthropogenic greenhouse gas emissions, although this approach also brings a novel set of climate changes and unknowns (Irvine et al., 2016; Robock et al., 2009). Among the most widely discussed proposals is stratospheric aerosol injection, in which particles or their precursors injected into the stratosphere reduce overall planetary albedo. Simulations with sulfate aerosol geoengineering demonstrate successful stabilization of global mean surface temperature despite increasing greenhouse gas concentrations (Ammann et al., 2010). Because many climate models do not include the relevant processes to reliably simulate more realistic approaches, an idealized scenario with reduced solar constant, known as sunshade geoengineering, is often studied in climate models as a simpler proxy for stratospheric aerosol injection (Kravitz et al., 2013). Reducing the solar constant does not offset the radiative forcing of increased CO_2 at each latitude separately, and thus, there are residual changes in

temperature at different latitudes (Kravitz et al., 2013; Moore et al., 2014; Russotto & Ackerman, 2018a), which have the potential to affect the general circulation.

The extratropical storm tracks, regions of heightened activity of extratropical cyclones, are an important feature of the general circulation that nonetheless remains understudied in the geoengineering literature. Extratropical cyclones are strongly associated with wind, temperature, and precipitation extremes (Shaw et al., 2016), and the storm tracks are the dominant contributor to poleward transport of energy in midlatitudes (Trenberth & Stepaniak, 2003). Furthermore, momentum convergence resulting from the storm tracks maintains surface westerlies (Peixoto & Oort, 1992), which help drive the ocean circulation and thus affect carbon and heat uptake. Variations in the storm tracks have also been shown to modulate ventilation of the boundary layer and thus affect air quality (Leibensperger et al., 2008).

Here, we analyze the response of the extratropical storm tracks in solar geoengineering scenarios. We use a simple metric of temporal variance in sea level pressure change, which we refer to as extratropical cyclone activity (ECA), to measure the general intensity of the storm tracks, although it does not distinguish between strength and frequency of individual storms. We chose ECA to use here based on data availability, but it has been shown to behave similarly to other metrics of cyclone activity based on winds and feature tracking for the climatological mean and the response to climate change (Chang et al., 2012; Chang et al., 2016).

We first examine experiment G1 of the Geoengineering Model Intercomparison Project (GeoMIP) (Kravitz et al., 2011), an idealized sunshade geoengineering experiment in which the solar constant is reduced to balance an instantaneous quadrupling of CO_2 relative to preindustrial concentrations. We also more briefly consider the changes in the storm tracks in two alternate experiments: the recently proposed "Half G1" experiment in which the solar constant is reduced by less than in G1 to avoid overcompensating effects on the climate system, and the Geoengineering Large Ensemble (GLENS). GLENS is an ensemble of simulations with CO_2 levels following representative concentration pathway 8.5 (RCP8.5) and SO_2 injections at four locations using a feedback-control algorithm (Tilmes et al., 2018). The aim of the feedback-control algorithm is to stabilize the meridional surface temperature gradient and interhemispheric surface temperature gradient in addition to global mean surface temperature (Kravitz et al., 2017). In GLENS, the northern and southern extratropical storm tracks weaken, and the southern storm track shifts poleward compared to present day (Richter et al., 2018; Simpson et al., 2019). Idealized experiments demonstrate that the poleward shift is due to stratospheric heating induced by the aerosols, but the general weakening is not well understood and cannot be attributed to stratospheric heating alone (Simpson et al., 2019). The GLENS simulations were designed to limit changes in the surface meridional temperature gradient at the planetary scale among other targets, but there are nonetheless substantial changes in meridional temperature gradients at midlatitudes (Tilmes et al., 2018), which could affect storm-track intensity.

To connect factors such as meridional temperature gradients to storm-track intensity, we use the concept of mean available potential energy (MAPE) (Lorenz, 1955). MAPE is the energy reservoir from which extratropical cyclones draw, and it is defined as the difference in integrated enthalpy between an atmosphere's mean state and the minimum-enthalpy state possible from reversible adiabatic parcel rearrangements (Lorenz, 1955, 1979). MAPE has been shown to scale linearly with the intensity of extratropical storm tracks as measured by eddy kinetic energy (Gertler & O'Gorman, 2019; O'Gorman, 2011; O'Gorman & Schneider, 2008; Schneider & Walker, 2008). MAPE can also be separated into nonconvective and convective components (Gertler & O'Gorman, 2019; O'Gorman, 2010). We focus on nonconvective MAPE, which is similar to MAPE but does not permit the release of convective instability through vertical reordering of air originating at a given latitude, because it has previously been found to scale more closely with storm-track intensity under forced changes to climate such as the seasonal cycle and global warming (Gertler & O'Gorman, 2019; O'Gorman, 2010). In general, MAPE increases with increasing meridional temperature gradients, decreasing dry static stability, and increasing specific humidity (Lorenz, 1955, 1979), and this allows us to reason about the effects of changes in these factors on storm-track intensity.

The paper proceeds as follows. In section 2, we introduce the model output and main analytical methods used in the paper. Section 3 details the changes in mean state and extratropical storm-track intensity in G1 and links them through MAPE. Section 4 gives an analysis of the storm-track response in GLENS and Half G1. Section 5 presents a discussion of the results and conclusions.

2. Simulations and Storm-Track Measures

2.1. Climate Models and Simulations

This study uses output from six climate models that performed the GeoMIP G1 experiment, the CMIP5 PI experiment, and the CMIP5 4xCO2 experiment. Grid sizes and references for each of the six models can be found in Supporting Information Table S1. While more than six models performed the G1 experiment, the models used here represent those with publicly available output necessary for the analyses described below.

In the G1 experiment, CO_2 concentrations are instantaneously quadrupled compared to preindustrial levels, and the solar constant is simultaneously reduced to counteract the resulting radiative imbalance at the top of atmosphere (Kravitz et al., 2011). The models are run for 50 years under these conditions, and to avoid transient effects in the first 10 years of the simulation, all results we present are based on time averages for the years 11–50, as is typical for the GeoMIP experiments (Kravitz et al., 2013). The CMIP5 PI experiment keeps CO_2 at preindustrial levels, and the 4xCO_2 experiment instantaneously quadruples CO_2 (Taylor et al., 2012), making these experiments natural comparisons to G1, as they represent a baseline and a global warming scenario, respectively. For purposes of comparison, 40-year averages are used from these experiments as well, based on years 11–50 of PI and 4xCO_2. For the 4xCO_2 experiment, equilibration would occur on much longer time scales than considered here, but the climate changes compared to PI are already large in years 11–50. We report the responses for G1 and 4xCO_2 relative to PI in all cases. The approach used to calculate changes under half-G1 is described in section 4.

This study also uses output from ensembles of simulations using the Community Earth System Model Version 1 with the Whole Atmosphere Community Climate Model as its atmospheric component, described in detail in Tilmes et al. (2018). The simulations have a latitudinal grid spacing of 0.9°, a longitudinal grid spacing of 1.25°, and 70 layers in the vertical, and they explicitly simulate the formation of sulfate aerosols from SO_2 injection. An ensemble of 19 simulations run from 2010 to 2030 with forcings following RCP8.5 is used as the control simulation (referred to as "BASE"). In GLENS, 19 simulations are run from year 2010 to 2099 with forcings following RCP8.5 and additional stratospheric SO_2 injections at four locations controlled by a feedback algorithm. Three of the BASE simulations were extended to 2095, and this smaller ensemble is used here as a global warming scenario for comparison (referred to as "RCP8.5"). Ensemble- and time-mean values over the 20-year period from 2076 to 2095 of the GLENS and RCP8.5 simulations are compared to ensemble- and time-mean values over the first 20 years of the BASE simulation in order to compare potential future climates to present day.

2.2. ECA

To estimate ECA, we use instantaneous daily sea level pressure (psl) for the GeoMIP experiments and six-hourly mean psl for the GLENS experiments to calculate the temporal variance of 24-hr psl change at each location (Chang et al., 2016),

$$\mathrm{ECA} = \overline{[\mathrm{psl}(t+24h) - psl(t)]^2},$$

where the overbar represents a time average over the period of interest, and psl(t + *24h)* is the sea level pressure 24 hours after a given time t. ECA is usually calculated using instantaneous 6-hourly psl, but these data were not available for most of the simulations used here. However, we confirmed that the results were very similar when instantaneous 6-hourly psl was used in a model for which it was available (IPSL-CM5A-LR). We also calculate an area-weighted mean of ECA over the extratropical latitude band 30°−70° in each hemisphere to give estimates of the overall ECA.

2.3. Calculation of MAPE

For the G1, PI, and 4xCO_2 experiments, zonal-mean temperature and humidity averaged over the 40-year periods described above are used to calculate MAPE and its nonconvective and convective components for each model individually. For the GLENS and BASE experiments, ensemble- and zonal-mean temperature and humidity averaged over the time periods described above are used. The zonal-mean temperatures and relative humidities in the 30°−70° latitude band in each hemisphere are interpolated to a 40 × 40 equal-area grid in latitude and pressure to create parcels of equal mass. Our conclusions are not sensitive

to this exact choice of latitude band. We use the divide-and-conquer algorithm (Stansifer et al., 2017) to find the minimum enthalpy state, and MAPE is then calculated as the difference between the enthalpy of the original state and that of the minimum-enthalpy state. The divide-and-conquer algorithm, while not exact, has been shown to be accurate for similar calculations to the ones performed here (Stansifer et al., 2017), and it can be adapted easily to calculate the nonconvective component of MAPE. To calculate nonconvective MAPE, a minimum-enthalpy state is found with the constraint that parcels originating from the same latitude cannot change their pressure ordering (see Gertler & O'Gorman, 2019 for further discussion). Convective MAPE is defined as the difference between MAPE and nonconvective MAPE.

3. Results for the G1 Experiment

3.1. Changes in Temperature and Humidity

The responses of temperature and meridional temperature gradient in G1 and 4xCO_2 relative to PI are shown in the model- and zonal-mean in Figure 1. Zonal-mean temperatures were interpolated onto a common grid (with grid spacings of 4° in latitude and 20 hPa in pressure) before meridional temperature gradients were calculated, and the mean across models was taken. Stippling indicates regions where fewer than five of six models agree on the sign of the response.

For G1, at high latitudes, there is warming in the lower troposphere with weaker cooling above roughly 650 hPa, and at low latitudes, there is cooling throughout the troposphere that is strongest in the upper troposphere consistent with a moist-adiabatic tropical stratification (Figure 1a). As a result, there is weakening of the meridional temperature gradient throughout the depth of the troposphere in the midlatitudes of both hemispheres (Figure 1c), which would tend to decrease MAPE and thus weaken the storm tracks. On the other hand, the dry static stability decreases in most regions (as can be inferred from Figure 1a), which would tend to increase MAPE and strengthen the storm tracks. The transition region from warming to cooling both at the surface and within the atmospheric column is somewhat uncertain, with different models transitioning in different areas (see Figure S1 for individual models).

For 4xCO_2, the meridional temperature gradient in the Northern Hemisphere weakens in the lower troposphere but strengthens above roughly 500 hPa (Figure 1d), and thus, the changes in meridional temperature gradient in the lower and upper troposphere would tend to have opposing effects on storm-track intensity. The Southern Hemisphere demonstrates changes of both signs in the meridional temperature gradient in the lower troposphere and stronger strengthening above 500 hPa (Figure 1d). The dry static stability decreases in the polar regions but increases at lower latitudes (as can be inferred from Figure 1b). The exact structure does again differ among individual models, but the general pattern is fairly robust (Figure S2).

The magnitudes of temperature changes for 4xCO_2 are generally larger than those for G1 by a factor of 5. However, the changes in meridional temperature gradients are closer in magnitude between 4xCO_2 and G1, and for the Northern Hemisphere, the inconsistent sign of the change in meridional temperature gradient at different levels for 4xCO_2 tends to reduce the magnitude of the overall effect on storm-track intensity. As a result, we will see later that the storm-track responses are of similar magnitude in the Northern Hemisphere for these two idealized scenarios.

The signs of the specific humidity responses are mostly as expected from the patterns of temperature change assuming small change in relative humidity (Figure S3). For G1, there are increases in specific humidity at lower latitudes and decreases at high latitudes in the lower troposphere with some intermodel differences in the pattern of changes (Figure S4). For 4xCO2, there are widespread increases in specific humidity consistently across models, which would tend to increase MAPE and storm-track intensity (Figure S5).

3.2. Changes in Extratropical Storm Tracks

As expected, given the changes in mean temperature structure and specific humidity, extratropical storm-track activity also changes in both the G1 and 4xCO_2 experiments. Figure 2 shows results for model-mean ECA versus latitude and longitude. ECA from each model was first interpolated onto a common grid (3° × 3° in latitude and longitude) before taking the mean across models. The extratropical storm tracks weaken in both hemispheres for G1 (Figure 2a), while the Northern Hemisphere storm track mostly

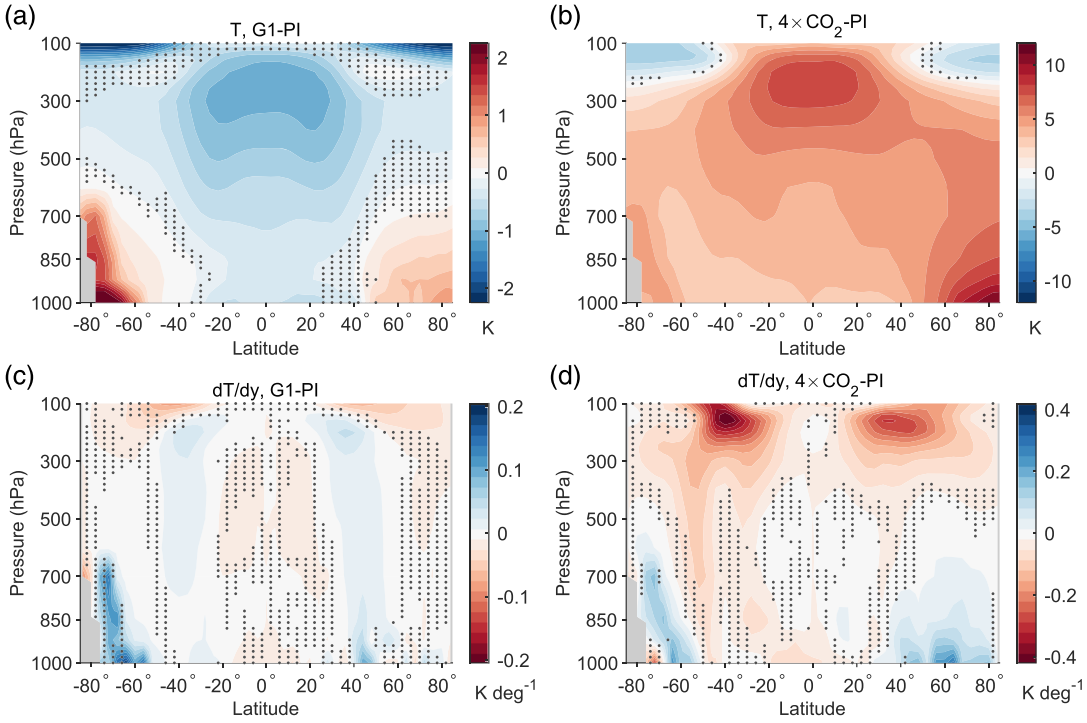

Figure 1. Model- and zonal-mean temperature and temperature gradient responses expressed as anomalies relative to PI. Shown are (a) temperature response for G1, (b) temperature response for 4xCO_2, (c) meridional temperature gradient response for G1, and (d) meridional temperature gradient response for 4xCO_2. Each panel has a different color bar, and stippling indicates regions where fewer than five of six models agree on sign of change. Temperature gradients are calculated in the equatorward direction in each hemisphere and are in units of K per degree latitude.

weakens and the Southern Hemisphere storm track strengthens and shifts poleward for 4xCO_2 (Figure 2b). For model-mean ECA, the strongest decrease in G1 is roughly four times smaller in magnitude compared to the strongest increase in 4xCO_2.

Figure 2d shows the model- and zonal-mean changes in ECA interpolated to a common grid with 0.1° resolution in latitude, making clear that decreases in ECA in the Northern Hemisphere are of similar magnitude in G1 and 4xCO_2. For the Southern Hemisphere under 4xCO_2, ECA increases are greater for latitudes poleward of the peak latitude of zonal-mean ECA in PI (Figure 2d), and this leads to a poleward shift in peak latitude of zonal-mean ECA by 3°. By contrast, the shifts in this peak latitude are small (<0.5°) in the Northern Hemisphere under 4xCO_2 and in both hemispheres under G1.

Some individual models demonstrate more heterogeneous storm-track changes (see Figures S6 and S7). For instance, in IPSL-CM5A and HadGEM2-ES, ECA increases in some regions of both the northern and southern storm tracks for G1. However, the average change over the extratropical latitude bands for G1 is always negative except for the Southern Hemisphere of HadGEM2-ES (see Figure 3a).

Storm-track changes in individual seasons are also more heterogeneous than changes in the annual mean (see Figures S8 and S9). Local seasonal variability in storm-track activity is important when considering the impacts of storm-track changes. Regions of ECA increases in G1 in winter and spring at high northern latitudes are generally consistent with the findings of Moore et al. (2014), which demonstrate increased cyclonic activity entering the Barents Sea in spring, affecting sea ice distribution. Nonetheless, in G1, the storm tracks always weaken on average in the extratropical latitude band in each hemisphere regardless of the season.

There are various possible metrics for storm-track activity, and ECA was chosen for this study based on data availability. ECA and eddy kinetic energy give broadly similar results in one model with sufficient data to compare, IPSL-CM5A (see Text S1).

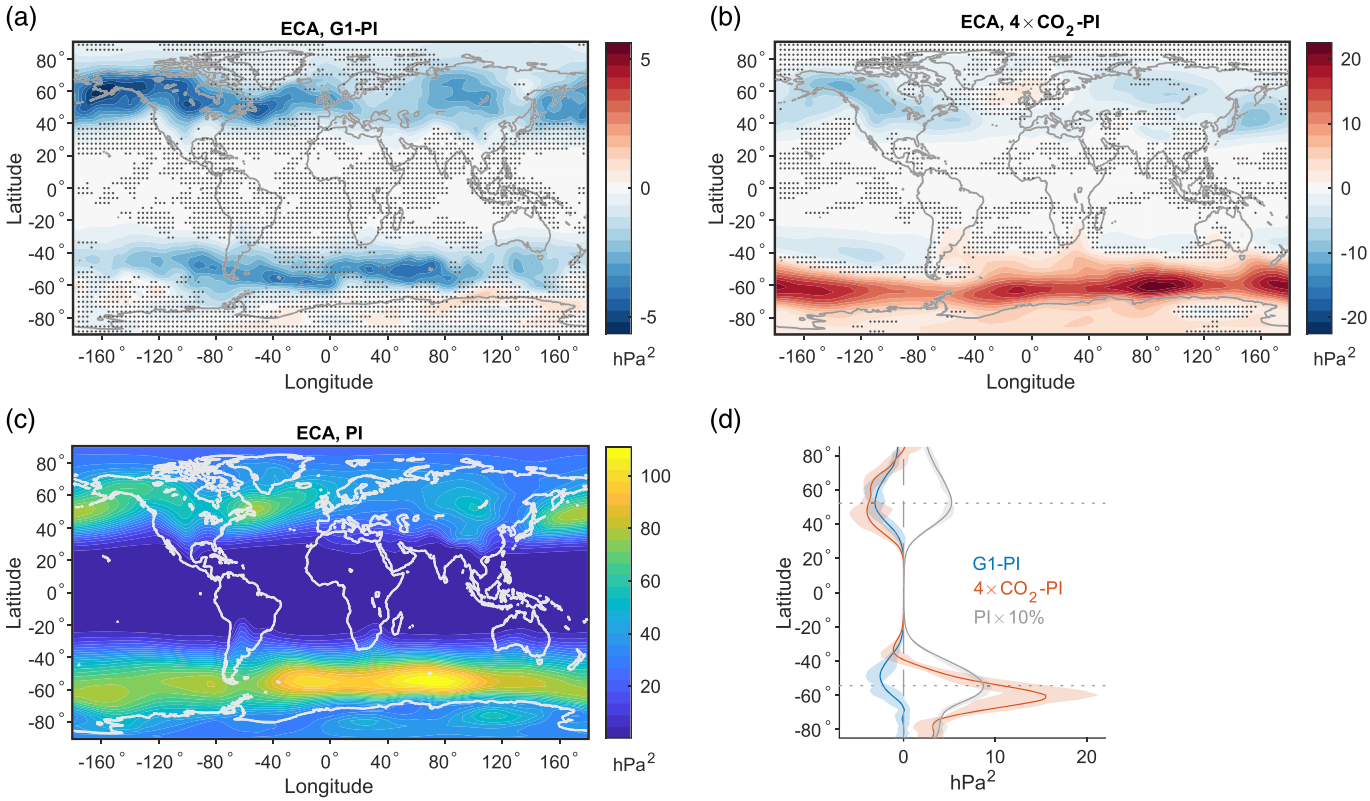

Figure 2. Model-mean storm-track intensity as measured by ECA. Shown are (a) response (expressed as anomalies relative to PI) for G1, (b) response for 4xCO_2, (c) PI climatology, and (d) zonal-mean responses for G1 (blue) and 4xCO_2 (red), and 10% of the PI climatological value (gray). Panels (a) and (b) have different color bars, and stippling in these panels indicates regions where fewer than five of six models agree on the sign of the response. Shading in (d) indicates range of inner four models (the second to the fifth sextiles), and horizontal dotted gray lines in (d) indicate latitudes of peak ECA in PI.

3.3. Changes in MAPE

We have shown that extratropical storm-track intensity weakens in both hemispheres under G1, and this seems consistent in sign with decreases in mean meridional temperature gradients in both hemispheres. However, the static stability and specific humidity also change, and the storm-track intensity in geoengineering scenarios could be affected by other factors such as changes in atmospheric longwave radiative cooling in response to increased CO_2 (Simpson et al., 2019). Therefore, it is important to address the question of whether the changes in storm-track intensity are quantitatively consistent with the changes in mean temperature and moisture. We address this question using the linear scaling of storm-track intensity with nonconvective MAPE that has been found in previous studies (Gertler & O'Gorman, 2019; O'Gorman, 2010).

Consistent with linear scaling, the fractional changes in nonconvective MAPE and ECA are broadly similar to each other in individual models and in the model mean, and within each hemisphere and idealized scenario (Figure 3). In the model mean of the northern extratropics, nonconvective MAPE decreases by 4.5% in G1 and by 7.9% in 4xCO_2, consistent with an ECA decrease by 5.2% in G1 and 8.2% in 4xCO_2. In the model mean of the southern extratropics, nonconvective MAPE decreases by 2.5% in G1 and increases by 8.7% in 4xCO_2, consistent with an ECA decrease by 2.6% in G1 and increase by 9.8% in 4xCO_2. These values are summarized in Table S2. The inner four of six models (second to fifth sextile) examined here are always consistent with the model-mean changes of sign in both ECA and nonconvective MAPE (Figure 3b).

Overall our comparison of changes in ECA and nonconvective MAPE suggests that changes in ECA in these idealized scenarios can be explained by changes in mean temperature and humidity. Replacing nonconvective MAPE with dry MAPE by specifying zero specific humidity gives qualitatively similar results, suggesting that temperature changes are the primary driver of changes in nonconvective MAPE and thus ECA. The convective component of MAPE increases by less under G1 as compared to 4xCO_2 for most models

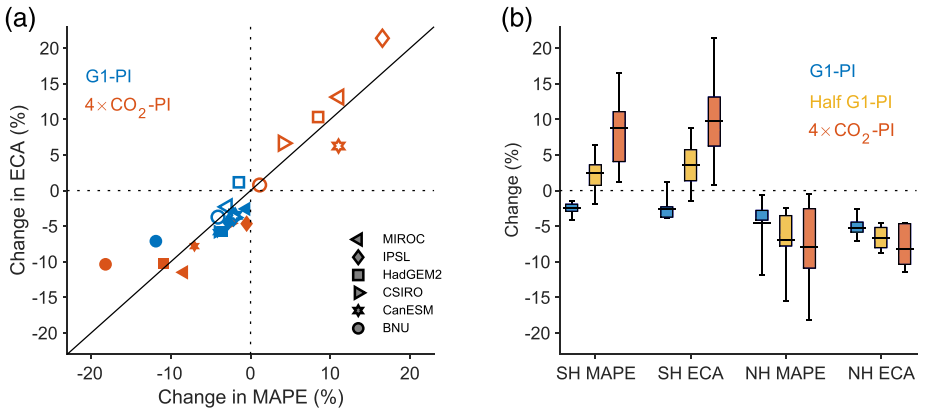

Figure 3. Extratropical storm-track intensity and nonconvective MAPE responses relative to PI for different scenarios and hemispheres. (a) Fractional changes in ECA versus fractional changes in nonconvective MAPE for G1 (blue) and 4xCO$_2$ (red) for the Northern Hemisphere (filled symbols) and Southern Hemisphere (open symbols) of individual models. The solid line is the one-to-one line. (b) Fractional changes for Southern Hemisphere (SH) and Northern Hemisphere (NH) nonconvective MAPE and ECA for G1 (blue), Half G1 (yellow), and 4xCO$_2$ (red). Boxes indicate range of inner four models (second to fifth sextiles), whiskers indicate maximum and minimum values, and midlines indicate model-mean values. All ECA values shown are averaged over 30°—70° latitude, and all MAPE values shown are calculated over 30°—70° latitude.

(Figure S10), which may imply less of an increase in the energy available for convection driven by ascent in extratropical cyclones.

4. Results for GLENS and Half-G1

For the more complex GLENS simulations with stratospheric SO_2 injection, we again consider average ECA over 30°–70° and MAPE calculated over 30°–70°, but now for GLENS and RCP8.5 compared to BASE. In GLENS, MAPE decreases by 14.9% and ECA decreases by 16.1% in the Northern Hemisphere, and MAPE decreases by 6.7% and ECA decreases by 7.8% in the Southern Hemisphere. These decreases in MAPE and ECA are consistent with decreases in the tropospheric meridional temperature gradient in both hemispheres (Figure S11). Ensemble-mean results for changes in ECA versus latitude and longitude are similar to the storm-track response reported in Simpson et al. (2019), with widespread weakening in both hemispheres (Figure S12). Thus, even in the more complex solar geoengineering simulations with feedback control and stratospheric SO_2 injection, a consistent weakening of the storm tracks occurs, and the changes in mean temperature and humidity alone are enough to explain the changes in storm track strength. In contrast to the multimodel mean for 4xCO$_2$, there is no overall strengthening of the storm track in the Southern Hemisphere in RCP8.5 for this ensemble and model (see Table S2), but the changes in ECA are still more negative in both hemispheres in GLENS as compared to RCP8.5.

We also consider the changes in ECA and MAPE in a "Half G1" scenario (Irvine et al., 2019), in which temperatures and relative humidities are linearly interpolated between the time-mean values for G1 and 4xCO2 at each grid cell such that global mean temperature is halfway between 4xCO$_2$ and G1. We then use these temperatures and relative humidities to calculate nonconvective MAPE. We also similarly interpolate ECA values at each grid cell, and results for ECA versus latitude and longitude in Half G1 can be seen in Figure S13. The results for changes in nonconvective MAPE and average ECA calculated over the 30°–70° latitude bands under Half G1 are shown in Figure 3b. In the Northern Hemisphere, nonconvective MAPE weakens by 6.9% and ECA weakens by 6.7% compared to PI in a Half G1 scenario, weakening that is of similar magnitude to the weakening under 4xCO$_2$. In the Southern Hemisphere, nonconvective MAPE strengthens by 2.5% and ECA strengthens by 3.6% under a Half G1 scenario, which is smaller than the strengthening under 4xCO$_2$. Unlike for some other aspects of the climate system, Half G1 fails to substantially reduce the change in storm-track intensity in the Northern Hemisphere, and this is because the Northern Hemisphere storm track weakens by similar amounts in G1 and 4xCO2. Thus, a half-geoengineering scenario would not substantially reduce the magnitude of storm-track changes in the Northern Hemisphere but would reduce them in the Southern Hemisphere.

5. Conclusions and Discussion

Changes to the mean temperature and humidity structure of the atmosphere under the G1 idealized geoengineering scenario reduce available potential energy in the northern and southern extratropics, leading to weakened extratropical storm tracks in both hemispheres with little change in their latitudinal position in the zonal mean. In the Northern Hemisphere, the storm track weakens by a comparable amount in G1 and 4xCO_2, despite the smaller changes in temperature in G1, in part because the meridional temperature gradient weakens at all levels in G1 but has offsetting changes of opposite sign in the upper and lower troposphere in 4xCO_2. In the Southern Hemisphere, the changes in storm-track intensity are smaller in magnitude in G1 than in 4xCO_2, but of opposite sign, and there is no poleward shift of the storm track in G1 unlike under 4xCO_2.

Given the importance of the extratropical storm tracks for both weather and climate (Shaw et al., 2016), their possible weakening should be considered when trying to explain the physical basis of changes in climate and the impacts of those changes under geoengineering. Weakening of the extratropical storm tracks would be expected to, for example, reduce wind extremes in midlatitudes but also possibly lead to less efficient ventilation of air pollution from the boundary layer (Leibensperger et al., 2008). A weakening of the storm tracks may also contribute to the decrease in low cloud fraction over the storm-track regions (Russotto & Ackerman, 2018b) and weakened poleward energy transport (Russotto & Ackerman, 2018a) identified previously in the G1 experiment.

It is reasonable to ask whether idealized sunshade geoengineering experiments are realistic or useful proxies for the type of solar geoengineering that is proposed as a possible intervention to global warming. However, we find that even experiments with stratospheric SO_2 injection demonstrate changes in temperature gradients and humidity that reduce available potential energy and weaken the storm tracks. There are nonetheless differences between the sunshade and stratospheric aerosol experiments analyzed in this paper, such as that stratospheric heating drives a poleward shift of the mean jet in the Southern Hemisphere in GLENS (Simpson et al., 2019) and to a lesser extent a poleward shift of the Southern Hemisphere storm track (Figure S12). Changes in both mean winds and the storm-track intensity near the coast of Antarctica in GLENS can affect mean surface wind stress and thus lead to changes in the wind-driven ocean circulation. Such changes in ocean circulation under geoengineering may in turn affect ice sheet stability as discussed in McCusker et al. (2015). However, there is little agreement among models on the sign of changes in storm-track strength in the Amundsen Sea sector, the region most crucial to West Antarctic ice sheet stability.

It is also reasonable to ask whether a geoengineering scenario in which the longwave radiative forcing from greenhouse gases is completely offset by engineered shortwave radiative forcing is the most reasonable or likely approach. In an idealized scenario representing roughly half of the reduction of solar radiation as compared to G1, changes in temperature and humidity still lead to a weakened storm track in the Northern Hemisphere of similar magnitude to the weakening in G1 and 4xCO_2. In the Southern Hemisphere, the storm-track intensity increases by less than under 4xCO_2, consistent with a smaller increase in MAPE. Further study of the storm-track response in less aggressive geoengineering scenarios would be of interest.

The study of solar geoengineering presents a unique scientific and social challenge for climate science: characterizing one unprecedented climate state, deliberate geoengineering, as a potential alternative to another unprecedented climate state, global warming incidental to anthropogenic activity. While there likely exist other consequences of solar geoengineering that the simulations studied here are unable to represent, our results for the storm tracks give examples of unintended consequences where solar geoengineering can fail to mitigate an aspect of climate change (in the Northern Hemisphere) or overcompensate for it (in the Southern Hemisphere).

Acknowledgments
We are grateful to R.G. Prinn for helpful discussions. C.G.G. was supported by the Industry and Foundation sponsors of the MIT Joint Program on the Science and Policy of Global Change, NASA grant NNX16AC98G to MIT, and the National Science Foundation Graduate Research Fellowship Program under NSF Grant 1122374. P. A.O'G. acknowledges support from NSF Grants AGS 1552195 and AGS 1749986. Support for B.K. was provided in part by the National Science Foundation through agreement CBET-1931641, the Indiana University Environmental Resilience Institute, and the *Prepared for Environmental Change* Grand Challenge initiative. The Pacific Northwest National Laboratory is operated for the US Department of Energy by Battelle Memorial Institute under contract DE-AC05-76RL01830. J. C.M. acknowledges support from the National Basic Research Program of China (2016YFA0602701). S.J.P. acknowledges support from the Australian Research Council's Special Research Initiative for the Antarctic Gateway Partnership (project SR140300001) and from CSIRO Oceans and Atmosphere. S.W. is supported by the "Integrated Research Program for Advancing Climate Models (TOUGOU Program)" from the Ministry of Education, Culture, Sports, Science, and Technology (MEXT), Japan. MIROC-ESM simulations were performed on the Earth Simulator at JAMSTEC. We are grateful to D. Ji for the BNU-ESM G1 model output (http://climatemodeling.bnu.edu.cn/G1.html). The other GeoMIP and CMIP5 data used in this study are available on the Earth System Grid (https://www.earthsystemgrid.org/). GLENS data and information are available at http://www.cesm.ucar.edu/projects/community-projects/GLENS/. A directory including all analysis code used in this study is published online at http://doi.org/10.5281/zenodo.3715447.

References

Ammann, C. M., Washington, W. M., Meehl, G. A., Buja, L., & Teng, H. Y. (2010). Climate engineering through artificial enhancement of natural forcings: Magnitudes and implied consequences. *Journal of Geophysical Research*, *115*, D22109. https://doi.org/10.1029/2009jd012878

Chang, E. K. M., Guo, Y. J., & Xia, X. M. (2012). CMIP5 multimodel ensemble projection of storm track change under global warming. *Journal of Geophysical Research*, *117*, D23118. https://doi.org/10.1029/2012jd018578

Chang, E. K. M., Ma, C. G., Zheng, C., & Yau, A. M. W. (2016). Observed and projected decrease in Northern Hemisphere extratropical cyclone activity in summer and its impacts on maximum temperature. *Geophysical Research Letters*, *43*, 2200–2208. https://doi.org/10.1002/2016gl068172

Gertler, C. G., & O'Gorman, P. A. (2019). Changing available energy for extratropical cyclones and associated convection in Northern Hemisphere summer. *Proceedings of the National Academy of Sciences*, *116*(10), 4105–4110. https://doi.org/10.1073/pnas.1812312116

Irvine, P. J., Emanuel, K., He, J., Horowitz, L. W., Vecchi, G., & Keith, D. (2019). Halving warming with idealized solar geoengineering moderates key climate hazards. *Nature Climate Change*, *9*(4), 295–299. https://doi.org/10.1038/s41558-019-0398-8

Irvine, P. J., Kravitz, B., Lawrence, M. G., & Muri, H. (2016). An overview of the Earth system science of solar geoengineering. *Wiley Interdisciplinary Reviews: Climate Change*, *7*(6), 815–833. https://doi.org/10.1002/wcc.423

Kravitz, B., Caldeira, K., Boucher, O., Robock, A., Rasch, P. J., Alterskjaer, K., et al. (2013). Climate model response from the Geoengineering Model Intercomparison Project (GeoMIP). *Journal of Geophysical Research: Atmospheres*, *118*, 8320–8332. https://doi.org/10.1002/jgrd.50646

Kravitz, B., MacMartin, D. G., Mills, M. J., Richter, J. H., Tilmes, S., Lamarque, J. F., et al. (2017). First simulations of designing stratospheric sulfate aerosol geoengineering to meet multiple simultaneous climate objectives. *Journal of Geophysical Research: Atmospheres*, *122*, 12,616–12,634. https://doi.org/10.1002/2017jd026874

Kravitz, B., Robock, A., Boucher, O., Schmidt, H., Taylor, K. E., Stenchikov, G., & Schulz, M. (2011). The Geoengineering Model Intercomparison Project (GeoMIP). *Atmospheric Science Letters*, *12*(2), 162–167. https://doi.org/10.1002/asl.316

Leibensperger, E. M., Mickley, L. J., & Jacob, D. J. (2008). Sensitivity of US air quality to mid-latitude cyclone frequency and implications of 1980-2006 climate change. *Atmospheric Chemistry and Physics*, *8*(23), 7075–7086. https://doi.org/10.5194/acp-8-7075-2008

Lorenz, E. N. (1955). Available potential energy and the maintenance of the general circulation. *Tellus*, *7*(2), 157–167.

Lorenz, E. N. (1979). Numerical evaluation of moist available energy. *Tellus*, *31*(3), 230–235.

McCusker, K. E., Battisti, D. S., & Bitz, C. M. (2015). Inability of stratospheric sulfate aerosol injections to preserve the West Antarctic ice sheet. *Geophysical Research Letters*, *42*, 4989–4997. https://doi.org/10.1002/2015gl064314

Moore, J. C., Rinke, A., Yu, X. Y., Ji, D. Y., Cui, X. F., Li, Y., et al. (2014). Arctic sea ice and atmospheric circulation under the GeoMIP G1 scenario. *Journal of Geophysical Research: Atmospheres*, *119*, 567–583. https://doi.org/10.1002/2013jd021060

O'Gorman, P. A. (2010). Understanding the varied response of the extratropical storm tracks to climate change. *Proceedings of the National Academy of Sciences*, *107*(45), 19176–19180. https://doi.org/10.1073/pnas.1011547107

O'Gorman, P. A. (2011). The effective static stability experienced by eddies in a moist atmosphere. *Journal of the Atmospheric Sciences*, *68*(1), 75–90. https://doi.org/10.1175/2010jas3537.1

O'Gorman, P. A., & Schneider, T. (2008). Energy of midlatitude transient eddies in idealized simulations of changed climates. *Journal of Climate*, *21*(22), 5797–5806. https://doi.org/10.1175/2008jcli2099.1

Peixoto, J. P., & Oort, A. H. (1992). *Physics of climate*. New York: American Institute of Physics.

Richter, J. H., Tilmes, S., Glanville, A., Kravitz, B., MacMartin, D. G., Mills, M. J., et al. (2018). Stratospheric response in the first geoengineering simulation meeting multiple surface climate objectives. *Journal of Geophysical Research: Atmospheres*, *123*, 5762–5782. https://doi.org/10.1029/2018jd028285

Robock, A., Marquardt, A., Kravitz, B., & Stenchikov, G. (2009). Benefits, risks, and costs of stratospheric geoengineering. *Geophysical Research Letters*, *36*, L19703. https://doi.org/10.1029/2009gl039209

Russotto, R. D., & Ackerman, T. P. (2018a). Energy transport, polar amplification, and ITCZ shifts in the GeoMIP G1 ensemble. *Atmospheric Chemistry and Physics*, *18*(3), 2287–2305. https://doi.org/10.5194/acp-18-2287-2018

Russotto, R. D., & Ackerman, T. P. (2018b). Changes in clouds and thermodynamics under solar geoengineering and implications for required solar reduction. *Atmospheric Chemistry and Physics*, *18*(16), 11,905–11,925. https://doi.org/10.5194/acp-18-11905-2018

Schneider, T., & Walker, C. C. (2008). Scaling laws and regime transitions of macroturbulence in dry atmospheres. *Journal of the Atmospheric Sciences*, *65*(7), 2153–2173. https://doi.org/10.1175/2007jas2616.1

Shaw, T. A., Baldwin, M., Barnes, E. A., Caballero, R., Garfinkel, C. I., Hwang, Y. T., et al. (2016). Storm track processes and the opposing influences of climate change. *Nature Geoscience*, *9*(9), 656–664. https://doi.org/10.1038/ngeo2783

Simpson, I. R., Tilmes, S., Richter, J. H., Kravitz, B., MacMartin, D. G., Mills, M. J., et al. (2019). The regional hydroclimate response to stratospheric sulfate geoengineering and the role of stratospheric heating. *Journal of Geophysical Research: Atmospheres*, *124*, 12,587–12,616. https://doi.org/10.1029/2019JD031093

Stansifer, E. M., O'Gorman, P. A., & Holt, J. I. (2017). Accurate computation of moist available potential energy with the Munkres algorithm. *Quarterly Journal of the Royal Meteorological Society*, *143*(702), 288–292. https://doi.org/10.1002/qj.2921

Taylor, K. E., Stouffer, R. J., & Meehl, G. A. (2012). An overview of CMIP5 and the experimental design. *Bulletin of the American Meteorological Society*, *93*(4), 485–498. https://doi.org/10.1175/bams-d-11-00094.1

Tilmes, S., Richter, J. H., Kravitz, B., MacMartin, D. G., Mills, M. J., Simpson, I. R., et al. (2018). CESMI (WACCM) stratospheric aerosol geoengineering large ensemble project. *Bulletin of the American Meteorological Society*, *99*(11), 2361–2371. https://doi.org/10.1175/bams-d-17-0267.1

Trenberth, K. E., & Stepaniak, D. P. (2003). Covariability of components of poleward atmospheric energy transports on seasonal and interannual timescales. *Journal of Climate*, *16*(22), 3691–3705. https://doi.org/10.1175/1520-0442(2003)016<3691:cocopa>2.0.co;2